

Parkes Pulsar Timing Array constraints on ultralight scalar-field dark matter

Nataliya K. Porayko,^{1,*} Xingjiang Zhu,^{2,3,4,†} Yuri Levin,^{5,6,2} Lam Hui,⁵ George Hobbs,⁷ Aleksandra Grudskaya,⁸ Konstantin Postnov,^{8,9} Matthew Bailes,^{10,4} N. D. Ramesh Bhat,¹¹ William Coles,¹² Shi Dai,⁷ James Dempsey,¹³ Michael J. Keith,¹⁴ Matthew Kerr,¹⁵ Michael Kramer,^{1,14} Paul D. Lasky,^{2,4} Richard N. Manchester,⁷ Stefan Osłowski,¹⁰ Aditya Parthasarathy,¹⁰ Vikram Ravi,¹⁶ Daniel J. Reardon,^{10,4} Pablo A. Rosado,¹⁰ Christopher J. Russell,¹⁷ Ryan M. Shannon,^{10,4} Renée Spiewak,¹⁰ Willem van Straten,¹⁸ Lawrence Toomey,⁷ Jingbo Wang,¹⁹ Linqing Wen,^{3,4} and Xiaopeng You²⁰

(PPTA Collaboration)

¹*Max-Planck-Institut für Radioastronomie, Auf dem Hügel 69, D-53121 Bonn, Germany*

²*School of Physics and Astronomy, Monash University, Clayton, VIC 3800, Australia*

³*School of Physics, University of Western Australia, Crawley, WA 6009, Australia*

⁴*OzGrav: Australian Research Council Centre of Excellence for Gravitational Wave Discovery, Hawthorn VIC 3122, Australia*

⁵*Center for Theoretical Physics, Department of Physics, Columbia University, New York, New York 10027, USA*

⁶*Center for Computational Astrophysics, Flatiron Institute, New York, New York 10010, USA*

⁷*CSIRO Astronomy and Space Science, P.O. Box 76, Epping, NSW 1710, Australia*

⁸*Sternberg Astronomical Institute, Lomonosov Moscow State University, Universitetskii pr. 13 Moscow 119234, Russia*

⁹*Kazan Federal University, Kremlevskaya 18, Kazan 420008, Russia*

¹⁰*Centre for Astrophysics and Supercomputing, Swinburne University of Technology, P.O. Box 218, Hawthorn, VIC 3122, Australia*

¹¹*International Centre for Radio Astronomy Research, Curtin University, Bentley, WA 6102, Australia*

¹²*Department of Electrical and Computer Engineering, University of California at San Diego, La Jolla, California 92093, USA*

¹³*CSIRO Information Management and Technology, PO Box 225, Dickson, ACT 2602, Australia*

¹⁴*Jodrell Bank Center for Astrophysics, University of Manchester, Manchester M13 9PL, UK*

¹⁵*Space Science Division, Naval Research Laboratory, Washington, DC 20375, USA*

¹⁶*Cahill Center for Astronomy and Astrophysics, MC 249-17, California Institute of Technology, Pasadena, California 91125, USA*

¹⁷*CSIRO Scientific Computing, Australian Technology Park, Locked Bag 9013, Alexandria, NSW 1435, Australia*

¹⁸*Institute for Radio Astronomy & Space Research, Auckland University of Technology, Private Bag 92006, Auckland 1142, New Zealand*

¹⁹*Xinjiang Astronomical Observatory, Chinese Academy of Sciences, 150 Science 1-Street, Urumqi, Xinjiang 830011, China*

²⁰*School of Physical Science and Technology, Southwest University, Chongqing 400715, China*



(Received 24 May 2018; published 5 November 2018)

It is widely accepted that dark matter contributes about a quarter of the critical mass-energy density in our Universe. The nature of dark matter is currently unknown, with the mass of possible constituents spanning nearly one hundred orders of magnitude. The ultralight scalar field dark matter, consisting of extremely light bosons with $m \sim 10^{-22}$ eV and often called “fuzzy” dark matter, provides intriguing solutions to some challenges at sub-Galactic scales for the standard cold dark matter model. As shown by Khmelnitsky and Rubakov, such a scalar field in the Galaxy would produce an oscillating gravitational potential with nanohertz frequencies, resulting in periodic variations in the times of arrival of radio pulses from pulsars. The Parkes Pulsar Timing Array (PPTA) has been monitoring 20 millisecond pulsars at two- to three-week intervals for more than a decade. In addition to the detection of nanohertz gravitational

*nporayko@mpifr-bonn.mpg.de

†xingjiang.zhu@monash.edu

waves, PPTA offers the opportunity for direct searches for fuzzy dark matter in an astrophysically feasible range of masses. We analyze the latest PPTA data set which includes timing observations for 26 pulsars made between 2004 and 2016. We perform a search in this data set for evidence of ultralight dark matter in the Galaxy using Bayesian and Frequentist methods. No statistically significant detection has been made. We, therefore, place upper limits on the local dark matter density. Our limits, improving on previous searches by a factor of 2 to 5, constrain the dark matter density of ultralight bosons with $m \leq 10^{-23}$ eV to be below 6 GeV cm^{-3} with 95% confidence in the Earth neighborhood. Finally, we discuss the prospect of probing the astrophysically favored mass range $m \gtrsim 10^{-22}$ eV with next-generation pulsar timing facilities.

DOI: [10.1103/PhysRevD.98.102002](https://doi.org/10.1103/PhysRevD.98.102002)

I. INTRODUCTION

Dark matter, a concept established in the early 1930s for the purpose of explaining the observed enigmatic dynamics of disk galaxies and motion of galaxies in clusters [1–3], is nowadays considered to be an essential ingredient of the Universe. It is instrumental in explaining a wide range of astrophysical phenomena, such as strong gravitational lensing of elliptical galaxies [4], the dynamics of interacting clusters [5] and the large-scale structure of the Universe [6]. The latest analysis of temperature and polarization anisotropies of the cosmic microwave background [7] suggested that the Universe contains 26% dark matter, which is five times more than ordinary baryonic matter such as stars and galaxies.

The most popular dark matter candidates are weakly interacting massive particles (WIMPs) and QCD (quantum chromodynamics) axions. We refer to both as standard cold dark matter, or simply CDM. The CDM paradigm has met with impressive success in matching observational data on large cosmological scales (see [8,9], for reviews). Recently, there has been an increased number of ideas about dark matter that go beyond the standard paradigm, building on old ideas in some cases (see e.g., [10] for an overview).

One such idea — an ultralight axion or axionlike particle — can be thought of as a generalization of the QCD axion. An axion is an angular field; i.e., the field range is finite and periodic with a periodicity $2\pi F_{\text{axion}}$ with F_{axion} often referred to as the axion decay constant. A simple axion Lagrangian has a standard kinetic term, and a self-interaction potential V generated by nonperturbative effects (that can be approximated by instanton potential),

$$V(\phi) = m^2 F_{\text{axion}}^2 [1 - \cos(\phi/F_{\text{axion}})], \quad (1)$$

where m is the mass of the axion ϕ . The nonperturbative effects are typically highly suppressed (e.g., exponentially suppressed by an instanton action), leading to a fairly low energy scale $\sqrt{mF_{\text{axion}}}$. In the early Universe, the scalar field is frozen at its primordial value, generically expected to be order of F_{axion} . When the Hubble expansion rate drops below the mass scale m , the scalar field oscillates with an amplitude that redshifts with the expansion of the Universe.

Averaging over oscillation cycles, ϕ behaves like CDM with a relic density of (see e.g., [11,12])¹

$$\Omega_{\text{axion}} \sim 0.1 \left(\frac{m}{10^{-22} \text{ eV}} \right)^{1/2} \left(\frac{F_{\text{axion}}}{10^{17} \text{ GeV}} \right)^2. \quad (2)$$

String theory contains many axion candidates with F_{axion} somewhere in the range 10^{16} – 10^{18} GeV [16]. Equation (2) tells us that a very low m is preferred if the axion were to account for dark matter. It should be emphasized though that there is a fairly large possible range for m ; in fact, the relic abundance is more sensitive to F_{axion} than to m . A lighter mass, e.g., $m \sim 10^{-23}$ eV, can be easily accommodated by a slightly higher F_{axion} , though it is disfavored by astrophysical observations such as the existence and structure of dwarf galaxies.²

Such an ultralight axion has a macroscopic de Broglie wavelength λ_{dB} , given by

$$\frac{\lambda_{\text{dB}}}{2\pi} = \frac{\hbar}{mv} \approx 60 \text{ pc} \left(\frac{10^{-22} \text{ eV}}{m} \right) \left(\frac{10^{-3} c}{v} \right), \quad (3)$$

where v is the velocity, implying wavelike phenomena on astronomically accessible scales, unlike standard CDM. In linear perturbation theory, the wavelike property leads to a suppression of power on small scales (small compared to the Jeans scale, which is a geometric mean of the Compton and Hubble scale). It is this property that motivated Hu, Barkana and Gruzinov [17] to propose an ultralight boson as an alternative to standard CDM, and to coin the term “fuzzy dark matter” (FDM). The term FDM refers generally to a scalar dark matter particle with a very small mass, such that its de Broglie wavelength is macroscopic. An ultralight axion is a particularly compelling realization. Our constraints derived in this paper apply to the ultralight axion, as well as the broader class of FDM.

The thinking was that the suppression of power on small scales would help resolve certain small scale problems of

¹The relic density computation follows the classic arguments of [13–15], which were developed for the QCD axion.

²Note that the requisite $\sqrt{mF_{\text{axion}}}$ is much less than the QCD scale; hence this is not the QCD axion.

CDM, which generally have to do with CDM predicting too much small-scale structure compared to that observed. There is a vast literature on this subject, but it remains a matter of debate as to whether the perceived small-scale structure problems of CDM are in fact amenable to astrophysical solutions (such as feedback processes modifying the mass distribution within Galactic halos); see [18] for a review.

There exist several different bounds on the FDM model. One class of bounds comes from measurements of the linear power spectrum at high redshifts, such as from the microwave background (e.g., [19]), and from the Lyman-alpha forest [20,21]. In particular, the Lyman-alpha forest data appear to disfavor a FDM mass lighter than about 10^{-21} eV. Another example of a bound of this kind come from 21-cm observations — the recent detection of a global 21-cm absorption signal at redshift around 18 [22] puts a lower limit on the FDM mass similar to the Lyman-alpha forest bound [23–25]. Yet another class of bounds comes from dynamical data on the density profiles of galaxies e.g., [26–28]. Many of these bounds are subject to their own astrophysical uncertainties. For instance, the Lyman-alpha forest bound is predicated upon the correct modeling of fluctuations from such as the ionizing background, the temperature and feedback processes. The 21-cm bound relies on assumptions about star formation (that it tracks the halo formation and that the fraction of baryons that form stars is less than about 5%), and of course assumes the validity of the detection. Constraints from rotation curve measurements generally make assumptions about how feedback processes, such as from stellar explosions, affect (or do not affect) density profiles.

Recently, a number of authors, based on numerical simulations and analytical arguments, pointed out additional testable astrophysical implications of FDM, especially in the nonlinear regime [12,29–33]. A particularly interesting probe of ultralight dark matter using pulsar timing arrays (PTAs) was pointed out by Khmelnitsky and Rubakov [34]. Through purely gravitational coupling, scalar field dark matter induces periodic oscillations in gravitational potentials with frequency twice the field mass $f \sim 2m \sim 5 \times 10^{-8} \text{ Hz}(m/10^{-22} \text{ eV})$. The oscillating gravitational potentials along the line of sight of pulsars cause sinusoidal variations in the times of arrival (ToAs) of radio pulses. The frequency of such variations lies right in the sensitivity band of PTAs. This way of detecting or constraining FDM is completely independent of other methods (and their assumptions), and provides a useful check. As shown in [34–37] and later in this paper, the current PTA data can only be sensitive to very low-mass FDM ($m < 10^{-23}$ eV). We will discuss what would be required to probe the higher and cosmologically more favorable masses.

The concept of a PTA is to regularly monitor ToAs of pulses from an array of the most rotationally stable

millisecond pulsars [38–41]. Measured ToAs are fitted with a deterministic timing model that accounts for the pulsar spin behavior and for the geometrical effects due to the motion of the pulsar and the Earth. The difference between the observed ToAs and those predicted by the best-fit timing model are called “timing residuals.” By analyzing the pulsar timing residuals, we can obtain the information about other physical processes that affect the propagation of radio pulses through the Galaxy, for instance, the presence of ultralight scalar field dark matter in the Galaxy.

The Parkes Pulsar Timing Array (PPTA) [42] uses the 64-m Parkes radio telescope in Australia. Building on earlier pulsar timing observations at Parkes, it started in 2005 to time 20 millisecond pulsars at a regular interval of two to three weeks. PPTA and its counterparts in North America (NANOGrav) [43] and Europe (EPTA) [44] have joined together to form the International Pulsar Timing Array (IPTA) [45,46], aiming for a more sensitive data set. The IPTA currently observes around 70 pulsars using the world’s most powerful radio telescopes.

The first PPTA data release was published in 2013 [42]. It included six years of observations for 20 pulsars. This data set was used to search for a stochastic gravitational wave (GW) background [47], continuous GWs [48] and GW bursts with memory [49]. The second data release is still being actively developed, but for this paper, we have made use of a data set that contains observations made between 2004 and 2016 with five new pulsars added since 2010. An early subset of this data was used to place the most constraining limit to date on the amplitude of a stochastic GW background in the nHz regime [50].

In this work we search for evidence of ultralight scalar field dark matter in the Galaxy using the PPTA data. A similar study was carried out, through Bayesian analysis, by Porayko and Postnov [35], using the NANOGrav 5-yr 17-pulsar data set published in [51]. Our work improves on that of [35] in several ways. First, we make use of an independent data set with much longer data span and smaller errors in the timing residuals. Second, we use an up-to-date Bayesian inference packages for PTA data analysis — PAL2 [52] and NX01 [53] — and include proper treatment of the noise processes. Reanalyzing the NANOGrav data with the improved analysis, we find that the sensitivity was overestimated by a factor of 10 in [35]. Third, we also adopt a standard Frequentist searching method and obtain consistent results with Bayesian analysis.

Our paper is organized as follows. In Sec. II, we describe pulsar timing residuals expected in the presence of ultralight scalar field dark matter in the Galaxy. In Sec. III, we introduce our data set, the likelihood function and our Bayesian and Frequentist methods to model the noise properties of PPTA data. We also present results of our noise analysis. In Sec. IV, we describe our search techniques and apply them to the PPTA data set. As we find no significant signals, we set upper limits on the local density

of FDM in the Galaxy. In Sec. V, we discuss how the sensitivity will be improved in the future. Finally, we provide concluding remarks in Sec. VI.

II. THE PULSAR TIMING RESIDUALS FROM FUZZY DARK MATTER

In this section we briefly describe the magnitude and time dependence of timing residuals induced by the scalar field dark matter in the Galaxy. A detailed derivation can be found in [34].

Because of the huge occupation number, the collection of ultralight dark matter particles behaves like a classical scalar field ϕ . To a very good approximation, here we ignore quartic self-interaction and coupling of ultralight dark matter particles to other fields³ [54]. The scalar action in this case can be written as

$$S_\phi = \int d^4x \sqrt{-g} \left[\frac{1}{2} g^{\mu\nu} D_\nu \phi D_\mu \phi - \frac{1}{2} m^2 \phi^2 \right], \quad (4)$$

to which the standard Einstein-Hilbert action for the metric should be added. The ϕ equation of motion is the Klein-Gordon-Fock Equation: $(\square_g + m^2)\phi(x) = 0$. We are interested in a computation of ϕ and the metric $g_{\mu\nu}$ inside the Galaxy. The metric is approximately Minkowski plus corrections at the level of 10^{-6} . To good approximation, ϕ everywhere in the Galaxy oscillates at an angular frequency mc^2/\hbar (corrections due to the momentum of the particles and the gravitational potential are small). The energy-momentum tensor to the leading-order is diagonal and its spatial components (pressure) oscillate at twice the field particle mass. This produces time-dependent gravitational potentials $g_{00} = 1 + 2\Phi(t)$ and $g_{ij} = -1 - 2\Psi(t)\delta_{ij}$ in the metric tensor (in the Newtonian covariant form) with leading oscillating contributions at a frequency

$$f = \frac{2mc^2}{h} \approx 4.8 \times 10^{-8} \left(\frac{m}{10^{-22} \text{ eV}} \right) \text{ Hz}. \quad (5)$$

The amplitude of oscillating parts of the potentials Ψ and Φ are a factor of $(v/c)^2$ smaller than the time-independent parts $\Phi_0 = -\Psi_0 \sim G\rho_{\text{SF}}\lambda_{\text{dB}}^2$, where ρ_{SF} is the local scalar field dark matter density. For cosmologically favored boson masses $\sim 10^{-22}$ eV, the frequency is fortuitously located in the sensitivity range of PTAs.

As in the case of GWs [39], pulsar photons propagating in a time-dependent metric undergo a frequency shift $\delta\nu$, which is related to timing residuals [34]

³In the axion context, the oscillation amplitude of ϕ gradually diminishes due to the expansion of the universe, making the quadratic $m^2\phi^2/2$ an excellent approximation to the potential in Eq. (1).

$$s(t) = \int_0^t \frac{\delta\nu}{\nu} dt = \frac{\Psi_c(x_e)}{2\pi f} \sin[2\pi f t + 2\alpha(x_e)] - \frac{\Psi_c(x_p)}{2\pi f} \sin \left[2\pi f \left(t - \frac{d_p}{c} \right) + 2\alpha(x_p) \right] + \left(\frac{\Psi + \Phi}{2\pi f} \right) \mathcal{O} \left(\frac{v}{c} \right), \quad (6)$$

where d_p is the distance to the pulsar and Ψ_c is the amplitude of cosine component of the oscillating part of the energy-momentum tensor. The subsequent terms in Eq. (6) are suppressed with respect to Ψ_c by a factor $v/c \simeq 10^{-3}$, and to the leading order, the signal $s(t)$ does not depend on the oscillating part of the potential Φ .

As one can see in Eq. (6), the dark matter signal also has ‘‘Earth’’ and ‘‘pulsar’’ terms. Oscillation frequencies at the Earth and at the pulsar are identical, which makes it analogous to the case of nonevolving continuous GWs [55]. The scalar-field oscillation phases on the Earth $\alpha(x_e)$ and pulsar $\alpha(x_p)$ generally take different values; but they become correlated when the Earth and a pulsar are located within the coherence de Broglie wavelength λ_{dB} .

The amplitude Ψ_c , which can be effectively probed in pulsar timing experiments, depends on the local density of dark matter ρ_{SF} ,

$$\Psi_c = \frac{G\rho_{\text{SF}}}{\pi f^2} \approx 6.1 \times 10^{-18} \left(\frac{m}{10^{-22} \text{ eV}} \right)^{-2} \left(\frac{\rho_{\text{SF}}}{\rho_0} \right), \quad (7)$$

where $\rho_0 = 0.4 \text{ GeV cm}^{-3}$ is the measured local dark matter density [56–58]. The root-mean-square (rms) amplitude of induced pulsar-timing residuals is

$$\delta t \approx 0.02 \text{ ns} \left(\frac{m}{10^{-22} \text{ eV}} \right)^{-3} \left(\frac{\rho_{\text{SF}}}{0.4 \text{ GeV cm}^{-3}} \right). \quad (8)$$

The expected signal amplitude scales strongly with the boson mass. At 10^{-22} eV and above, the signal is negligibly small. For mass below 10^{-23} eV, the induced rms residuals ($\gtrsim 20$ ns) are comparable to current timing precision for the best pulsars, as we discuss in Sec. III A.

In this work, we assume the Earth term and pulsar terms have the same amplitude Ψ_c . This is a reasonable approximation since most PPTA pulsars are relatively close ($\lesssim 1$ kpc) to the Earth (see Table I). We discuss effects of the dark matter density variability in Sec. V. Under this assumption, Eq. (6) can be written into a more compact form,

$$s(t) = \frac{\Psi_c}{\pi f} \sin(\alpha_e - \theta_p) \cos(2\pi f t + \alpha_e + \theta_p), \quad (9)$$

where we have defined $\alpha_e = \alpha(x_e)$ and $\theta_p = \alpha_p - \pi f d_p/c$ with $\alpha_p = \alpha(x_p)$. Defining θ_p this way allows us searching for a single phase parameter per pulsar. One should note,

TABLE I. Key characteristics of the PPTA data set: σ — median ToA uncertainty, rms — weighted root-mean-square of timing residuals, T_{obs} — data span and its start and end months (Range), N_{obs} — number of observations, d_p — pulsar distance taken from the ATNF Pulsar Catalogue [59].

Pulsar name	σ (μs)	rms (μs)	T_{obs} (yr)	Range	N_{obs}	d_p (kpc)
J0437–4715	0.15	0.15	11.98	2004.02–2016.01	3820	0.16
J0613–0200	1.20	1.38	11.98	2004.02–2016.01	969	0.78
J0711–6830	3.29	1.58	11.98	2004.02–2016.01	1017	0.11
J1017–7156	0.97	0.76	5.54	2010.07–2016.01	524	0.26
J1022+1001	2.23	2.11	11.98	2004.02–2016.01	1008	1.13
J1024–0719	3.39	3.61	11.87	2004.02–2015.12	679	1.22
J1045–4509	3.82	3.35	11.98	2004.02–2016.01	854	0.34
J1125–6014	1.59	1.29	10.12	2005.12–2016.01	203	0.99
J1446–4701	1.81	1.47	5.19	2010.11–2016.01	161	1.57
J1545–4550	1.08	1.01	4.74	2011.05–2016.01	215	2.25
J1600–3053	0.91	0.71	11.98	2004.02–2016.01	969	1.80
J1603–7202	2.13	1.43	11.98	2004.02–2016.01	747	0.53
J1643–1224	1.75	2.96	11.98	2004.02–2016.01	713	0.74
J1713+0747	0.38	0.24	11.98	2004.02–2016.01	880	1.18
J1730–2304	2.01	1.48	11.98	2004.02–2016.02	655	0.62
J1732–5049	2.55	2.75	7.23	2004.03–2011.12	144	1.87
J1744–1134	0.68	0.61	11.98	2004.02–2016.01	855	0.40
J1824–2452A	2.67	16.5	10.36	2005.05–2015.10	339	5.50
J1832–0836	0.53	0.25	2.86	2012.11–2015.10	68	0.81
J1857+0943	2.00	1.93	11.98	2004.02–2016.01	580	1.20
J1909–3744	0.25	0.16	11.98	2004.02–2016.01	1670	1.14
J1939+2134	0.36	1.43	11.87	2004.03–2016.01	591	3.50
J2124–3358	4.67	2.52	11.98	2004.02–2016.01	889	0.41
J2129–5721	1.82	1.19	11.65	2004.06–2016.01	540	3.20
J2145–0750	1.71	1.16	11.86	2004.03–2016.01	881	0.53
J2241–5236	0.44	0.28	5.98	2010.02–2016.01	615	0.96

however, that the parameter pair (α_e, θ_p) is indistinguishable from $(\alpha_e \pm \pi, \theta_p \pm \pi)$.

III. PPTA DATA AND NOISE PROPERTIES

A. Observations and timing analysis

Here we provide a brief overview of the data set used in this work. The data set is available from the CSIRO pulsar data archive.⁴ The observing systems and data processing techniques are similar to the first data release (DR1) as described in Ref. [42]. Table I summarizes key characteristics of the PPTA data set, including the median ToA uncertainties, weighted rms values of timing residuals, data spans and the number of observations.

Our data set consists of observations for 26 pulsars collected between February 5, 2004, and January 31, 2016, using the Parkes telescope. It includes DR1 data that were acquired between March 2005 and March 2011 for 20 pulsars, along with some earlier data for some pulsars that were observed in the 20-cm observing band prior to the official start of the PPTA project. Currently, the PPTA

observes 25 pulsars, with PSR J1732–5049 having been removed from the pulsar sample in 2011 because we were unable to obtain high quality data sets for this pulsar. The observing cadence is normally once every two to three weeks. In each session, every pulsar was observed in three radio bands (10, 20 and 50 cm) with a typical integration time of one hour. Twenty of these pulsars were monitored for more than ten years up to twelve years; only five pulsars have data spans less than five years. For this data set, the median ToA uncertainties vary from 149 ns (PSR J0437–4715) to 4.67 μs (PSR J2124–3358); the weighted rms residuals in this data set vary from 152 ns (PSR J0437–4715) to 16.53 μs (PSR J1824–2452A). PSRs J1939+2134 and J1824–2452A were excluded from the search analysis, as they show strong evidence for a large unmodeled red-noise component.⁵ For our purpose, we find these two pulsars make little contribution to the sensitivity.

⁴<https://doi.org/10.4225/08/5aff8174e9b3>.

⁵This is evident as their rms residuals are much larger than the median ToA uncertainties given in Table I. This may be accounted for using system- and band-specific noise terms [60].

During pulsar timing observations, ToAs are first referred to a local hydrogen maser frequency standard at the observatory. These ToAs are further transformed to coordinated universal time (UTC) and then to a terrestrial time (TT) as published by the Bureau International des Poids et Mesures. For the current data set, we used TT (BIPM2015) and adopted the JPL DE418 [61] solar system ephemeris (SSE) model to project ToAs to the solar-system barycenter. Potential errors in SSE models are accounted for in our Bayesian analysis (Sec. IV A).

Before performing the search for dark matter signals, we fit pulsar ToAs with a timing model using the standard TEMPO2 software package [62,63]. Typical parameters included in this fit are the pulsar sky location (RAJ and DecJ), spin frequency and spin-down rate, dispersion measure, proper motion, parallax and (when applicable) binary orbital parameters. Additionally, constant offsets or jumps were fitted among ToAs collected with different receiver/backend systems. Below we describe our methods to estimate the noise properties of the PPTA data.

B. The likelihood function

The likelihood function for pulsar timing residuals, marginalized over the m timing model parameters, can be written as [64,65]

$$\mathcal{L}(\boldsymbol{\vartheta}, \boldsymbol{\psi} | \boldsymbol{\delta t}) = \frac{(M^T C^{-1} M)^{-1}}{\sqrt{(2\pi)^{n-m} \det C}} \times \exp \left[-\frac{1}{2} (\boldsymbol{\delta t} - \boldsymbol{s}')^T C' (\boldsymbol{\delta t} - \boldsymbol{s}') \right], \quad (10)$$

where $\boldsymbol{\delta t}$ is a vector of timing residuals with length n , \boldsymbol{s}' is the deterministic signal vector, including the dark matter signal as described in Sec. II and deterministic systematics, M is the $(n \times m)$ design matrix or regression matrix of the linear model [66] that describes how ToAs depend on timing model parameters.⁶ The noise covariance matrix $C = C_{\text{WN}} + C_{\text{SN}} + C_{\text{DM}}$ includes contributions from uncorrelated white noise (C_{WN}), time-correlated spin noise (C_{SN}) and dispersion measure variations (C_{DM}). In Eq. (10), we have defined $C' = C^{-1} - C^{-1} M (M^T C^{-1} M)^{-1} M^T C^{-1}$. The covariance matrix C depends on the set of noise parameters $\boldsymbol{\vartheta}$, and $\boldsymbol{\psi}$ denotes deterministic signal parameters so that $\boldsymbol{s}' = \boldsymbol{s}'(\boldsymbol{\psi})$. As a result, this form of the likelihood, which was first implemented in [64], depends both on $\boldsymbol{\vartheta}$ and $\boldsymbol{\psi}$, and provides the possibility of proper treatment of the signal in the presence of correlated noise and systematics. The likelihood in Eq. (10) can be further reduced to a more compact form (see Ref. [65] for details),

$$\mathcal{L}(\boldsymbol{\vartheta}, \boldsymbol{\psi} | \boldsymbol{\delta t}) = \frac{1}{\sqrt{(2\pi)^{n-m} \det(G^T C G)}} \times \exp \left[-\frac{1}{2} (\boldsymbol{\delta t} - \boldsymbol{s}')^T G (G^T C G)^{-1} G^T (\boldsymbol{\delta t} - \boldsymbol{s}') \right], \quad (11)$$

where the $n \times (n - m)$ dimension matrix G is obtained through the singular-value decomposition of the design matrix M . Specifically, $M = USV^*$ where U and V are unitary matrices with $n \times n$ and $m \times m$ dimension respectively, and S is an $n \times m$ diagonal matrix containing singular values of M . The G matrix is obtained such that $U = (U_1 G)$ with U_1 and G consisting of the first m and the remaining $n - m$ columns of U , respectively.

In this work, we assume that only the dark matter signal, noise processes (that will be described in the next subsection) and deterministic systematics, associated with SSE errors, contribute to the data. We neglect errors in terrestrial time standards and other common noise processes (such as a stochastic GW background). Therefore, the likelihood function for the full PTA can be expressed as a product:

$$\mathcal{L}(\boldsymbol{\vartheta}, \boldsymbol{\psi} | \boldsymbol{\delta t}) = \prod_{i=1}^{N_p} \mathcal{L}(\boldsymbol{\vartheta}_i, \boldsymbol{\psi}_i | \boldsymbol{\delta t}_i), \quad (12)$$

where N_p is the number of pulsars in the timing array.

C. Noise modeling

For each pulsar in the PPTA data set, we estimate its noise properties using both Bayesian and Frequentist approaches. We present a general description of possible noise sources here.

Stochastic noise processes can be divided into the time-correlated and uncorrelated components. The uncorrelated (white) noise is represented by the uncertainties of the measured ToAs derived through cross-correlation of the pulsar template and the integrated profile. However, it is common that ToA uncertainties underestimate the white noise present in pulsar timing data. This might be caused by, e.g., radio frequency interference, pulse profile changes or instrumental artifacts. Two parameters, namely, EFAC (Error FACtor) and EQUAD (Error added in QUADrature), are included to account for excess white noise. They are introduced for each observing system used in the data set. Following standard conventions, different parameterizations are used for EFAC and EQUAD. In TEMPO2 and for our Frequentist analysis, the re-scaled ToA uncertainties (σ_s) are related to their original values (σ) by

$$\sigma_s^2 = \text{T2EFAC}^2 (\sigma^2 + \text{T2EQUAD}^2). \quad (13)$$

In Bayesian analysis, we use the following relation

$$\sigma_s^2 = (\text{EFAC} \sigma)^2 + \text{EQUAD}^2. \quad (14)$$

⁶It can be obtained with the TEMPO2 `designmatrix` plugin.

TABLE II. List of parameters and prior distributions used for the Bayesian analysis. U and log-U stand for uniform and log-uniform priors, respectively.

Parameter	Description	Prior	Comments
Noise parameters (Θ)			
EFAC	White-noise modifier per backend	U [0, 10]	Fixed for setting limits
EQUAD	Additive white noise per backend	log-U [-10, -4]	Fixed for setting limits
A_{SN}	Spin-noise amplitude	log-U [-20, -11] (search) U [10^{-20} , 10^{-11}] (limit)	One parameter per pulsar
γ_{SN}	Spin-noise spectral index	U [0, 7]	One parameter per pulsar
A_{DM}	DM-noise amplitude	log-U [-20, -6.5] (search) U [10^{-20} , $10^{-6.5}$] (limit)	One parameter per pulsar
γ_{DM}	DM-noise spectral index	U [0, 7]	One parameter per pulsar
Signal parameters (Ψ)			
Ψ_c	Oscillation amplitude	log-U [-20, -12] (search) U [10^{-20} , 10^{-12}] (limit)	One parameter per PTA
α_e	Oscillation phase on Earth	U [0, 2π]	One parameter per PTA
θ_p	$\theta_p = \alpha_p - \pi f d_p / c$	U [0, 2π]	One parameter per pulsar
f (Hz)	Oscillation frequency	log-U [-9, -7]	Delta function for setting limits
BayesEphem parameters (Ψ^{sys})			
z_{drift}	Drift-rate of Earth's orbit about ecliptic z-axis	U [-10^{-9} , 10^{-9}] rad yr $^{-1}$	One parameter per PTA
$\Delta M_{\text{jupiter}}$	Perturbation of Jupiter's mass	$\mathcal{N}(0, 1.5 \times 10^{-11}) M_{\odot}$	One parameter per PTA
$\Delta M_{\text{saturan}}$	Perturbation of Saturn's mass	$\mathcal{N}(0, 8.2 \times 10^{-12}) M_{\odot}$	One parameter per PTA
ΔM_{uranus}	Perturbation of Uranus' mass	$\mathcal{N}(0, 5.7 \times 10^{-11}) M_{\odot}$	One parameter per PTA
$\Delta M_{\text{neptune}}$	Perturbation of Neptune's mass	$\mathcal{N}(0, 7.9 \times 10^{-11}) M_{\odot}$	One parameter per PTA
PCA_i	Principal components of Jupiter's orbit	U [-0.05, 0.05]	Six parameters per PTA

Numerous studies [67–69] have found evidence for additional low-frequency noise in pulsar timing data. This time-correlated stochastic process is dominated by two components: *achromatic* (i.e., independent of radio frequency) spin noise and *chromatic* (i.e., dependent on radio frequency) such as dispersion measure (DM) variations. The former is intrinsic to the pulsar and might be related to pulsar rotational instabilities. The latter is associated with the interstellar medium which introduces time delays in pulsar ToAs. As pulsar travels in the tangent plane, the line of sight intersects spatially variable interstellar medium characterized by different column electron densities. For current receivers, the bandpass is generally not broad enough to resolve these kind of variations in each individual observation. Therefore, a typical strategy is to observe pulsars at widely separated radio bands, allowing the correction of DM variations.

Below we discuss details of noise modeling in the Bayesian and Frequentist frameworks.

1. Bayesian framework

The Bayesian framework provides a consistent approach to the estimation of a set of parameters Θ by updating the initial distribution of those parameters $P_{\text{pr}}(\Theta)$ as more information becomes available. Bayes' theorem states:

$$P_{\text{pst}}(\Theta|\mathbf{D}) = \frac{\mathcal{L}(\Theta|\mathbf{D})P_{\text{pr}}(\Theta)}{Z}, \quad (15)$$

where $P_{\text{pst}}(\Theta|\mathbf{D})$ stands for the posterior (or updated) distribution of the parameters Θ , given the data (or external information) \mathbf{D} , $\mathcal{L}(\Theta|\mathbf{D})$ is the likelihood function, and Z is known as Bayesian evidence and defined as:

$$Z = \int \mathcal{L}(\Theta|\mathbf{D})P_{\text{pr}}(\Theta)d^n(\Theta) \quad (16)$$

The Bayesian evidence is a normalizing factor for parameter estimation problem and is a key criterion for model selection and decision making. Here Z does not depend on Θ and it holds that $P_{\text{pst}}(\Theta|\mathbf{D}) \propto \mathcal{L}(\Theta|\mathbf{D})P_{\text{pr}}(\Theta)$. When applied for the case of PTAs, data \mathbf{D} includes an array of pulsar timing ToAs δt , Θ includes $[\vartheta, \psi]$ and the likelihood $\mathcal{L}(\Theta|\mathbf{D})$ is given by Eq. (10). The set of parameters, used for the Bayesian analysis, and the corresponding priors are described in Table II.

For computational purposes, the noise covariance matrix C from Eq. (10) can be split as a sum of a diagonal matrix C_{WN} and a large dense matrix $K = C_{\text{SN}} + C_{\text{DM}} = F\Phi F^T$, where $\Phi = \Phi_{\text{SN}} + \Phi_{\text{DM}}$ is the diagonal matrix ($2k \times 2k$), $k \ll n$, where k is the number of terms in the approximation sum. By using the Woodbury matrix lemma⁷ [70], the

⁷ $(N + F\Phi F^T)^{-1} = N^{-1} - N^{-1}F(\Phi^{-1} + F^T N^{-1}F)^{-1}F^T N^{-1}$.

computationally heavy inversion of covariance matrix C , involving $\mathcal{O}(n^3)$ operations, is reduced to lower rank diagonal matrix inversion Φ^{-1} . More details on this technique can be found in [71,72].

In this work we have used the so-called ‘‘Fourier-sum’’ prescription (or ‘‘time-frequency’’ method), introduced in [73]. In this case, the Fourier transform matrix F for achromatic processes can be written as:

$$\mathbf{F} = (\mathbf{F}^s \mathbf{F}^c), \quad F_{ji}^s = \sin(2\pi\nu_i t_j), \quad F_{ji}^c = \cos(2\pi\nu_i t_j), \quad (17)$$

where $\nu_i = i/T$, where T is the whole timespan of the PPTA data set, 11.98 years. The dimensionality of the Fourier matrix F is $(n \times 2k)$, where k is number of frequency components, which in our case is 30. The noise vector for a specific noise process can be expressed as $\tau_j = \sum_i F_{ji} a_i = \sum_i a_i^s \sin 2\pi\nu_i t_j + a_i^c \cos 2\pi\nu_i t_j$, where $\mathbf{a} = (\mathbf{a}^s, \mathbf{a}^c)$ is the vector of Fourier coefficients.

The covariance matrix of Fourier coefficients Φ can be derived from the covariance matrix of the theoretical power spectrum of a specific type of noise. Within Bayesian framework, we use the following parametrization for power-law noise:

$$P(f) = \frac{A^2}{12\pi^2} \text{yr}^3 \left(\frac{f}{\text{yr}^{-1}} \right)^{-\gamma}. \quad (18)$$

Therefore, the elements of the matrix Φ , which are identical for both spin and DM noises, are expressed as:

$$\Phi_{ij} = \frac{A^2}{12\pi^2} \frac{\nu_i^{-\gamma}}{T} \text{yr}^3 \delta_{ij}, \quad (19)$$

where i, j iterates over different Fourier frequencies and δ_{ij} is a Kronecker delta. If multiband observations are available, the degeneracy between the spin noise and DM contributions can be broken, because of the dependency of the amplitude of the DM variations on the observational frequency f_o . This dependency enters in the Fourier transform matrix as:

$$\mathbf{F}_{\text{DM}} = (\mathbf{F}_{\text{DM}}^s \mathbf{F}_{\text{DM}}^c), \quad F_{\text{DM},ji}^s = \frac{\sin(2\pi\nu_i t_j)}{K f_{o,j}^2}, \quad F_{\text{DM},ji}^c = \frac{\cos(2\pi\nu_i t_j)}{K f_{o,j}^2}, \quad (20)$$

where $K = 2.41 \times 10^{-16} \text{ Hz}^{-2} \text{ cm}^{-3} \text{ pc s}^{-1}$ and $f_{o,j}$ is the radio observing frequency at time t_j . Using this terminology, the time delay δt between signal received at radio frequency f_0 and one received at $f \rightarrow \infty$ is given by $\delta t = K^{-1} f_0^{-2} \text{DM} = 4.15 \times 10^6 f_0^{-2} \text{DM ms}$. Note that the linear and quadratic trends in DM variations get absorbed by timing model parameters DM1 and DM2, which are included in the Bayesian timing model. The inclusion of the

DM derivatives in our analysis absolves us from the spectral leakage problem [74].

The formalism, described in this subsection, was implemented in a range of publicly available codes. For the single pulsar analysis we have used PAL2 Software — a package for the Bayesian processing of the pulsar timing data. Efficient sampling from the posteriors is performed by the Bayesian inference tool MULTINEST [75], running in constant efficiency mode — a computational technique that allows one to maintain the user-defined sampling efficiency for high-dimensional problems (see Ref. [76] for more details). For each PPTA pulsar we perform separately a full noise modeling analysis, simultaneously including all stochastic components discussed above. The noise parameters \mathfrak{P} , estimated within single pulsar analysis, are given in Table III. The marginalized posterior probabilities for the six most sensitive pulsars in PPTA (see Sec. IV A) are presented in Appendix B.

As was shown in [77,78], and later confirmed in [60], data for PSR J1603 – 7202 and PSR J1713 + 0747 show significant evidence for nonstationary extreme scattering events (ESEs), which are usually associated with the passage of high density plasma ‘‘blobs’’ along the line of sight of a pulsar. ESEs are modeled as deterministic signals $t_{\text{ESE},i}$ [60]:

$$t_{\text{ESE},i} = \frac{\mathcal{S}(t_i, \mathbf{A}_{\text{ESE}}, \mathcal{W})}{K f_{o,i}^2}, \quad (21)$$

by making use of shapelet basis function expansion:

$$\begin{aligned} \mathcal{S}(t, \mathbf{A}_{\text{ESE}}, \mathcal{W}) &= \sum_{j=0}^{j_{\text{max}}} A_{\text{ESE},j} B_j(t, \mathcal{W}), \\ B_j(t, \mathcal{W}) &= [2^j j! \mathcal{W} \sqrt{\pi}]^{-1/2} H_j \left(\frac{t - t_0}{\mathcal{W}} \right) \\ &\times \exp \left[-\frac{(t - t_0)^2}{2\mathcal{W}^2} \right], \end{aligned} \quad (22)$$

where t_0 is the epoch of ESE, \mathcal{W} stands for the characteristic length scale of ESE, H_j is the j -th Hermitian polynomial, j_{max} is the number of terms used in the expansion, which is 3 in our case, \mathbf{A}_{ESE} is a vector of shapelet amplitudes. The inclusion of nonstationary ESEs in the noise model (see Table III) leads to smaller DM spectral amplitudes A_{DM} and slightly steeper slopes, characterised by γ_{DM} , which is consistent with results presented in [60].

2. Frequentist methods

In the Frequentist framework, we use the method that was originally introduced in [79] and further improved in [77] for correcting DM variations. The basic idea works as

TABLE III. Noise properties of PPTA pulsars, determined through Bayesian and Frequentist analyses. The comparison of the results for intrinsic spin noise determined via two methods, can be performed when $f_c T \ll 1$, such as $P_0 \rightarrow A_{SN}^2 / (12\pi^2 f_c^2)$. Dashed lines indicate either that noise parameters are not constrained, i.e., flat posterior probabilities (Bayesian) or that no spin noise is detected (Frequentist). In the two “note” columns, C is for “constrained” distributions, whereas SC stands for “semiconstrained” distributions which exhibit long tails and significant deviation from Gaussianity (possibly due to correlation with other parameters); See Fig. 7 in Appendix B for illustrations. The last two rows list results when parameters for nonstationary ESEs are included. Only pulsars with a † symbol next to their names are used for setting Bayesian upper limits.

Pulsar name	Bayesian						Frequentist		
	$\log 10(A_{SN})$	γ_{SN}	Note	$\log 10(A_{DM})$	γ_{DM}	Note	α	f_c (yr ⁻¹)	P_0 (yr ³)
J0437–4715†	$-13.96_{-0.05}^{+0.05}$	$2.0_{-0.2}^{+0.2}$	C	$-10.90_{-0.04}^{+0.04}$	$3.2_{-0.2}^{+0.2}$	C	3.5	0.08	2.37×10^{-27}
J0613–0200	$-16.89_{-1.9}^{+1.9}$	$3.4_{-2.0}^{+2.0}$	SC	$-10.62_{-0.05}^{+0.05}$	$2.1_{-0.3}^{+0.3}$	C	2.5	0.08	1.30×10^{-26}
J0711–6830	$-14.1_{-0.4}^{+0.5}$	$4.2_{-1.1}^{+1.2}$	C	$-12.1_{-1.7}^{+0.8}$	$3.9_{-1.7}^{+1.6}$	SC	4.0	0.08	3.98×10^{-26}
J1017–7156	$-13.5_{-0.6}^{+0.3}$	$3.6_{-1.5}^{+1.9}$	C	$-10.12_{-0.06}^{+0.06}$	$3.2_{-0.4}^{+0.4}$	C	6.0	1.0	9.54×10^{-28}
J1022+1001	$-16.9_{-1.7}^{+2.4}$	$2.9_{-2.0}^{+2.1}$	SC	$-11.3_{-0.4}^{+0.3}$	$3.2_{-0.8}^{+1.2}$	C	2.0	0.08	3.04×10^{-26}
J1024–0719	$-14.6_{-0.5}^{+0.4}$	$6.1_{-0.9}^{+0.6}$	SC	$-11.6_{-0.6}^{+0.4}$	$4.2_{-1.2}^{+1.3}$	C	3.0	0.08	4.30×10^{-25}
J1045–4509	$-12.85_{-0.5}^{+0.2}$	$2.0_{-0.6}^{+1.1}$	C	$-9.73_{-0.04}^{+0.04}$	$2.8_{-0.3}^{+0.3}$	C	3.0	0.3	7.44×10^{-27}
J1125–6014	$-14.5_{-0.4}^{+0.4}$	$6.0_{-0.7}^{+0.7}$	C	$-11.6_{-0.5}^{+0.5}$	$4.3_{-1.2}^{+1.1}$	C	3.0	0.2	5.79×10^{-27}
J1446–4701
J1545–4550		$-10.8_{-0.4}^{+0.3}$	$4.6_{-1.3}^{+1.3}$	C	3.0	0.1	1.66×10^{-26}
J1600–3053†	$-16.8_{-1.9}^{+1.7}$	$3.3_{-1.9}^{+2.1}$	SC	$-10.6_{-0.09}^{+0.08}$	$2.7_{-0.3}^{+0.3}$	C	2.0	0.08	1.05×10^{-27}
J1603–7202	$-13.3_{-0.5}^{+0.2}$	$2.4_{-0.7}^{+1.2}$	C	$-10.20_{-0.05}^{+0.05}$	$2.5_{-0.3}^{+0.3}$	C	3.0	0.08	8.39×10^{-26}
J1643–1224	$-12.40_{-0.05}^{+0.05}$	$1.5_{-0.3}^{+0.4}$	C	$-9.81_{-0.04}^{+0.04}$	$1.6_{-0.3}^{+0.3}$	C	1.5	0.08	3.43×10^{-26}
J1713+0747	$-13.5_{-0.1}^{+0.1}$	$2.4_{-0.3}^{+0.3}$	C	$-10.79_{-0.06}^{+0.07}$	$1.7_{-0.3}^{+0.3}$	C
J1730–2304	$-17.2_{-1.7}^{+1.7}$	$3.2_{-2.0}^{+2.0}$	C	$-11.2_{-0.4}^{+0.3}$	$3.6_{-0.7}^{+0.9}$	C	2.0	0.08	2.17×10^{-26}
J1732–5049	$-16.1_{-2.3}^{+2.3}$	$3.3_{-1.9}^{+2.1}$	SC	$-10.6_{-5.7}^{+0.6}$	$3.2_{-1.3}^{+1.7}$	SC
J1744–1134†	$-13.33_{-0.06}^{+0.06}$	$1.2_{-0.3}^{+0.3}$	SC	$-11.5_{-0.5}^{+0.3}$	$3.3_{-0.7}^{+1.2}$	SC	6.0	1.0	2.55×10^{-28}
J1824–2452A	$-12.60_{-0.12}^{+0.07}$	$3.7_{-0.4}^{+1.4}$	SC	$-9.74_{-0.06}^{+0.07}$	$2.5_{-0.4}^{+0.4}$	C	4.0	0.1	1.22×10^{-23}
J1832–0836
J1857+0943	$-15.1_{-2.4}^{+1.1}$	$4.0_{-2.0}^{+1.7}$	SC	$-10.6_{-0.2}^{+0.1}$	$2.3_{-0.5}^{+0.5}$	C
J1909–3744†	$-14.5_{-0.7}^{+0.5}$	$2.4_{-0.8}^{+1.1}$	C	$-11.09_{-0.04}^{+0.04}$	$1.6_{-0.2}^{+0.3}$	C	2.5	0.07	7.54×10^{-28}
J1939+2134	$-13.34_{-0.2}^{+0.1}$	$3.2_{-0.4}^{+0.6}$	C	$-10.25_{-0.04}^{+0.04}$	$3.1_{-1.5}^{+1.8}$	C	4.0	0.08	2.50×10^{-25}
J2124–3358		$-11.9_{-4.5}^{+0.9}$	$2.8_{-0.9}^{+0.9}$	SC	5.0	1.0	5.64×10^{-27}
J2129–5721	$-16.9_{-1.8}^{+1.8}$	$3.2_{-2.0}^{+2.0}$	SC	$-10.9_{-0.1}^{+0.1}$	$2.3_{-0.5}^{+0.5}$	C	2	0.08	1.37×10^{-26}
J2145–0750	$-13.04_{-0.06}^{+0.06}$	$1.4_{-0.2}^{+0.2}$	C	$-11.1_{-0.2}^{+0.2}$	$2.9_{-0.6}^{+0.6}$	C	1.0	0.08	5.13×10^{-27}
J2241–5236†	$-13.48_{-0.1}^{+0.08}$	$1.4_{-0.5}^{+0.6}$	C	$-12.8_{-4.8}^{+1.0}$	$3.9_{-2.4}^{+2.1}$	SC
Including extreme scattering events									
J1603–7202	$-13.3_{-0.2}^{+0.2}$	$2.3_{-0.6}^{+0.5}$	C	$-10.55_{-0.08}^{+0.08}$	$2.6_{-0.3}^{+0.3}$	C			
J1713+0747†	$-13.50_{-0.08}^{+0.08}$	$2.3_{-0.3}^{+0.3}$	C	$-11.2_{-0.1}^{+0.1}$	$2.5_{-0.4}^{+0.4}$	C			

follows. Timing residuals are separated into two components, one dependent on the radio wavelength, namely, dispersion measure variations — DM(t), and the other independent of the radio wavelength. The latter could

contain red noise, GWs or dark matter signals. Since pulsar timing data are irregularly sampled, we use a linear interpolation scheme to estimate DM(t) at regular intervals. For the PPTA data, we estimate one DM(t) every 60-180 days using

observations taken at three bands (10, 20, 50 cm). The time epochs and the estimated DM offsets are stored as DMOFF parameters in the TEMPO2 .par files. We model the red spin noise on data that have been corrected for DM variations, in which case, the noise covariance matrix contains only the white noise and spin noise terms.

Following the TEMPO2 convention, for our Frequentist analysis the intrinsic spin noise is parameterized using the following power-law spectrum

$$P(f) = \frac{P_0}{[1 + (\frac{f}{f_c})^2]^{\alpha/2}}, \quad (23)$$

where P_0 is an overall amplitude (normally expressed in yr^3), f_c is the so-called corner frequency, α is the power-law exponent. The covariance matrix for such a red noise process is given by

$$\begin{aligned} \mathcal{C}(\tau) &= \int_0^\infty P(f) \cos \tau f df \\ &= \frac{2^{(1-\alpha)/2} P_0 \sqrt{\pi} \tau^{(\alpha-1)/2} J_{\frac{1-\alpha}{2}}(f_c \tau)}{f_c^{-(1+\alpha)/2} \Gamma(\frac{\alpha}{2})}, \end{aligned} \quad (24)$$

where $\tau = 2\pi|t_i - t_j|$ with t_i and t_j being the ToA at the i th and j th observation, respectively, J is the modified Bessel function of second kind and Γ is the Gamma function.

We follow the method described in [80] to estimate red noise properties iteratively. We fit a power-law model of the form given by Eq. (23) to the power spectrum of timing residuals, leading to an initial estimate of the noise covariance matrix. We then use the Cholesky decomposition of this matrix to transform the data. The power spectrum of the transformed residuals should be white. We repeat the above procedure to obtain improved estimates of the spectrum. The iteration is considered converged if the whitened data show a sufficiently flat spectrum for which the spectral leakage is not dominant. The results are usually validated with simulations. We list our best estimates of red noise parameters in Table III.

IV. SEARCH TECHNIQUES AND RESULTS

A. Bayesian analysis

Within a Bayesian framework, the signal detection problem is addressed through model selection. Given the observational data, we wish to choose between two mutually exclusive hypotheses: the null hypothesis \mathcal{H}_0 that the signal is absent and the alternative hypothesis \mathcal{H}_1 that the signal is present. We compute the evidences \mathcal{Z} , defined in Eq. (16), of the two hypotheses, \mathcal{H}_0 and \mathcal{H}_1 . Assuming *a priori* equal probability for both hypotheses, the following evidence ratio (commonly called Bayes factor) quantifies the support of \mathcal{H}_1 against \mathcal{H}_0 ,

$$\mathcal{B} = \frac{\mathcal{Z}_1}{\mathcal{Z}_0} = \frac{\int \mathcal{L}(\boldsymbol{\vartheta}, \boldsymbol{\psi}, \boldsymbol{\psi}^{\text{sys}} | \delta t) P_{\text{pr}}(\boldsymbol{\vartheta}, \boldsymbol{\psi}, \boldsymbol{\psi}^{\text{sys}}) d\boldsymbol{\vartheta} d\boldsymbol{\psi}^{\text{sys}} d\boldsymbol{\psi}}{\int \mathcal{L}(\boldsymbol{\vartheta}, \boldsymbol{\psi}^{\text{sys}} | \delta t) P_{\text{pr}}(\boldsymbol{\vartheta}, \boldsymbol{\psi}^{\text{sys}}) d\boldsymbol{\vartheta} d\boldsymbol{\psi}^{\text{sys}}}, \quad (25)$$

where $\boldsymbol{\psi}^{\text{sys}}$ are the parameters of the deterministic systematics, SSE errors in our case, which should be distinguished from dark matter signal parameters $\boldsymbol{\psi}$. In order to obtain accurate evidence estimates, we carry out numerical integration via MULTINEST with enabled importance nested sampling in constant efficiency mode. With the current PPTA data, we find a log Bayes factor $\ln \mathcal{B}$ of 2.1 in the frequency range $[10^{-9}, 8 \times 10^{-8}]$ Hz, implying that our data are consistent with containing only noise. When we extend the search frequency to 10^{-7} Hz, the signal hypothesis is favored against the null hypothesis with $\ln \mathcal{B} = 70$. We suspect this is caused by the unmodeled perturbations of the mass and orbital elements of Mercury, for which the synodic period is ~ 116 days, corresponding to a frequency of 10^{-7} Hz. We defer the investigation of this feature to a future work.

In order to set an upper limit on the signal amplitude within the Bayesian framework, we perform the parameter estimation routine. By sampling from the posterior probabilities of model parameters, we can numerically marginalize over nuisance parameters, and get the posterior distribution for the amplitude Ψ_c . We define the 95% Bayesian upper limit $\bar{\Psi}_c$, such that 95% of the samples from the posterior probability lie within the range $[0, \bar{\Psi}_c]$:

$$\begin{aligned} 0.95 &= \int_0^{\bar{\Psi}_c} d\Psi_c \int d\boldsymbol{\psi}' d\boldsymbol{\vartheta} \mathcal{L}(\Psi_c, \boldsymbol{\psi}', \boldsymbol{\vartheta} | \delta t) P_{\text{pr}}(\Psi_c) \\ &\quad \times P_{\text{pr}}(\boldsymbol{\psi}') P_{\text{pr}}(\boldsymbol{\vartheta}). \end{aligned} \quad (26)$$

We split the frequency range between 10^{-9} and 10^{-7} Hz into a number of small bins and find $\bar{\Psi}_c$ for each bin separately.

To reduce the computational costs of numerical marginalization, a common practice is to fix the noise model parameters to their maximum likelihood values [72,81], determined from single pulsar analysis. However, such a procedure can possibly lead to upper limits biased by a factor of $\lesssim 2$ [72]. In this work we allow both signal and correlated noise parameters to vary simultaneously. The white noise EFACs and EQUADs, which should have little or no correlation with dark matter parameters, are fixed to the maximum-likelihood values obtained from single pulsar analysis.

Recently, it was shown that the search for a stochastic GW background can be seriously affected by the uncertainties in the SSE [82,83]. We employ a physical model BayesEphem to account for the SSE uncertainties that are most relevant for pulsar timing. The BayesEphem model has 11 parameters, including 4 parameters which describe

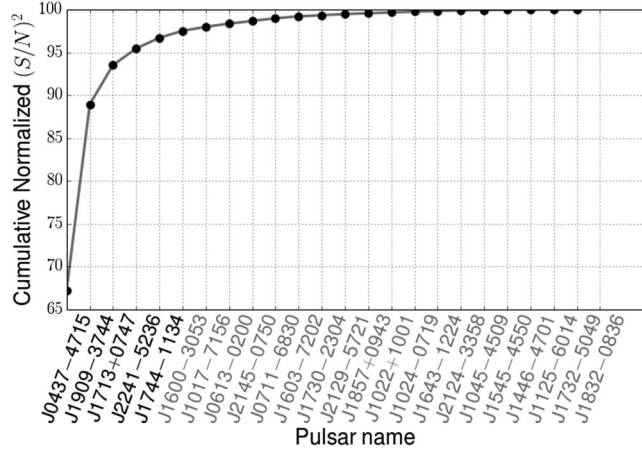


FIG. 1. Cumulative normalized $(S/N)^2$. The pulsars are ranked according to their contribution to the PPTA sensitivity between $5 \times 10^{-9} - 2 \times 10^{-8}$ Hz (see text for details).

the perturbations in the masses of outer planets, 1 parameter which is associated with the uncertainty in the semi-major axis of Earth-Moon barycenter orbit, and 6 parameters that characterize the perturbation of the Earth’s orbit due to errors in the Jovian average orbital elements. The `BayesEphem` modeling technique is described in [82] in detail, and implemented in publicly available software packages, such as `enterprise` and `NX01`. The latter was used to put robust constraints on the amplitude of the FDM in this work.

The number of free parameters for the PPTA data set is $5 \times N_p + 3 + 11 = 144$ (see Table II), where N_p is the number of pulsars in PTA. In order to further reduce the computational costs, we have formed the “restricted data set” by choosing the five best pulsars. As shown in Fig. 1, they contribute to more than 95% sensitivity of the full PPTA. Here pulsars are ranked according to their contribution to the squared signal-to-noise ratio $(S/N)^2$; see Eq. (29) in the next section. We carry out the calculations by adding detectable signals to 1000 noise realizations, sampled from individual pulsar noise posterior distribution obtained in Sec. III C 1.

1. Validation of the search results

In order to validate our upper limits and test the robustness of our algorithms, we have injected a signal with $f = 2 \times 10^{-9}$ Hz and amplitude $\Psi_c = 10^{-14}$ into our restricted data set. At this frequency, the amplitude of the injected signal is comparable to the Bayesian upper limit. In order to recover this signal, we run the full Bayesian analysis, simultaneously accounting for both dark matter signal and noise. The posterior probabilities are demonstrated in Fig. 2, indicating successful recovery of the injected signal.

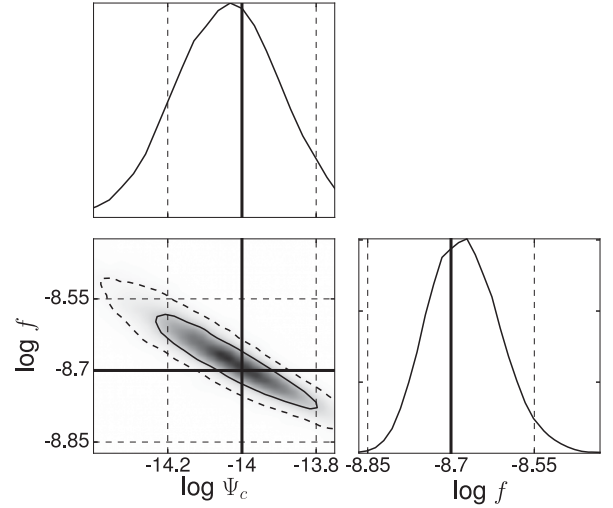


FIG. 2. The marginalized posterior distributions for the amplitude Ψ_c and frequency f for a signal injection in the actual PPTA data. The thick black lines mark the injected values and the contours are 1- and 2- σ credible regions.

B. Frequentist analysis

In a Frequentist framework, signal detection is essentially a statistical hypothesis testing problem; we wish to choose between the null hypothesis \mathcal{H}_0 and the signal hypothesis \mathcal{H}_1 based on the observations. The task is to find an optimal statistic that maximizes the signal detection probability at a fixed false alarm probability. Following the Neyman-Pearson criterion, the log-likelihood ratio is an optimal statistic,

$$\ln \Lambda \equiv \ln \frac{\mathcal{L}(\mathcal{H}_1 | \delta \mathbf{t})}{\mathcal{L}(\mathcal{H}_0 | \delta \mathbf{t})} = \sum_{i=1}^{N_p} \left[(\delta \mathbf{t}_i | \mathbf{s}_i) - \frac{1}{2} (\mathbf{s}_i | \mathbf{s}_i) \right], \quad (27)$$

where we have used Eqs. (11) and (12) to derive the second equality above, and the inner product between two time series \mathbf{x} and \mathbf{y} is defined as

$$(\mathbf{x} | \mathbf{y}) = \mathbf{x}^T G (G^T C G)^{-1} G^T \mathbf{y}. \quad (28)$$

It is useful to define the signal-to-noise ratio in the following form,

$$S/N = \sqrt{2 \langle \ln \Lambda \rangle} = \left[\sum_{i=1}^{N_p} (\mathbf{s}_i | \mathbf{s}_i) \right]^{1/2}, \quad (29)$$

where $\langle \dots \rangle$ stands for the expectation value over a large number of noise realizations. In this work, we adopt $2 \ln \Lambda$ as our detection statistic. For our Frequentist analysis, noise model parameters are fixed at their maximum likelihood values. The signal parameters in question are: the amplitude of dark matter induced gravitational-potential oscillations

Ψ_c , oscillation frequency f , phase parameters α_e and θ_p ; see Eq. (9). It turns out that the statistic can be analytically maximized over Ψ_c and thus the parameter space that needs to be numerically searched over is $N_p + 2$ dimensional. For our data, this corresponds to 28 dimensions, making a grid-based search unfeasible. We employ the particle swarm optimization technique [84], which has been demonstrated to be very effective for searches for continuous GWs with PTAs [55,85]. The detection statistic follows a χ^2 distribution with one degree of freedom for noise-only data.

Since we find no evidence for statistically significant signals in the data, which is consistent with results from the Bayesian analysis as described in the previous subsection, we set upper limits on the dimensionless amplitude Ψ_c . We compute the 95% confidence upper limits for a number of frequency bins between 10^{-9} and 10^{-7} Hz. At each frequency, we compute the S/N for 10^3 simulated signals with random phase parameters and a fixed Ψ_c . The 95% confidence upper limit on Ψ_c corresponds to the amplitude at which 95% of signals result in $S/N \geq 2.4$. Here the S/N threshold is chosen such that the expectation value for our detection statistic in the presence of signals, given by $1 + (S/N)^2$, is greater than the detection threshold that corresponds to 1% false alarm probability. It implies that: if there was a signal with an amplitude higher than $\bar{\Psi}_c$ present in the data, it would have been detectable with more than 95% probability.

C. Upper limits

Figure 3 shows the 95% upper limits on the amplitude Ψ_c , calculated within Bayesian (black solid line) and frequentist frameworks (purple solid line). As one can see, Bayesian upper limits are a factor of 2–3 worse than frequentist upper limits in the low-frequency regime, while in the mid-to-high frequency range, both methods produce comparable results. The difference might be predominantly attributed to the covariance between signal and noise (especially the red spin noise). Frequentist upper limits were calculated by fixing noise parameters at their maximum likelihood values, whereas we search simultaneously over signal and noise parameters in the Bayesian analysis.

The Bayesian upper limits, obtained with 5-year NANOGrav data set [51], are also plotted as the thin dash-dotted (taken from [35]) and dashed (recalculated in this paper) lines. We note that upper limits presented in Ref. [35] were underestimated by a factor of 10 due to the less conservative⁸ choice of prior (log-uniform) probability of the amplitude Ψ_c , as well as the noninclusion of DM variations and additional white noise terms (EFAC and EQUAD). From Fig. 3, one can see that our data set is

⁸We note that uniform priors result in upper limits that are a factor of ~ 5 higher than log-uniform priors.

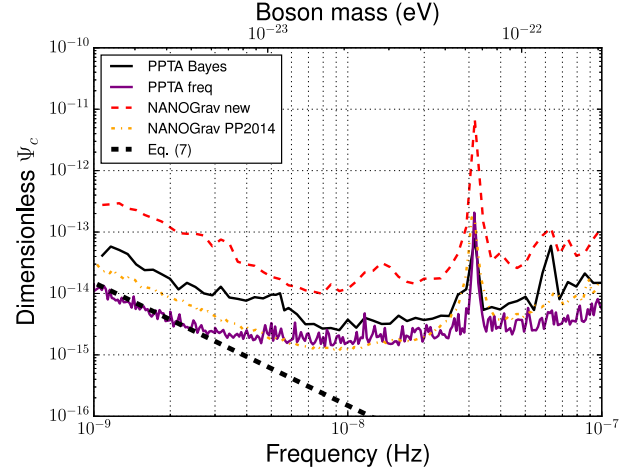


FIG. 3. Upper limits on the signal amplitude Ψ_c , generated by the scalar field dark matter in the Galaxy, as a function of frequency (boson mass). The purple solid line shows results from Frequentist analysis of the full data set of 24 pulsars, while the black solid line demonstrates the upper limits derived within a Bayesian framework (only the five best pulsars were used). These are compared with previous studies using the NANOGrav 5-yr data set: dash-dotted orange — upper limits set in [35], dashed red — upper limits recalculated in this work. The thick black dashed line shows the model amplitude Ψ_c , assuming $\rho_{\text{SF}} = 0.4 \text{ GeV cm}^{-3}$, given by Eq. (7).

a factor of 5 more sensitive to the dark matter signal than NANOGrav 5-year data at low frequencies, corresponding to boson masses $m \lesssim 10^{-23} \text{ eV}$. In the intermediate regime, the improvement is about a factor of 2. This is expected because of our much longer data span and higher observing cadence. It is interesting to note that the upper limit curves in Fig. 3 exhibit similar frequency dependencies to the sky-averaged upper limits for continuous GWs (see, e.g., [48]). In Appendix A, we present Frequentist upper limits obtained by including in the analysis only Earth terms. We also show how Bayesian upper limits are modified if different fixed SSE models are used.

V. FUTURE PROSPECTS

In this section, we discuss the future improvement in sensitivity of PTAs to the dark matter signal. In particular, the five-hundred-meter aperture spherical telescope (FAST [86]) in China, MeerKAT [87] — a precursor for the planned Square Kilometre Array (SKA [88]) — and ultimately the SKA, are expected to significantly increase the sensitivities of PTAs. With broad frequency bands and massive collecting areas, the radiometer noise for some of the brightest pulsars can be reduced from current 100 ns level down to below 10 ns [89]. However, it might be too optimistic to assume a white noise level of 10 ns because of the so-called jitter

TABLE IV. White noise for 10 PPTA pulsars in the FAST/SKA era.

Pulsar name	σ_r (ns)	σ_J (ns)	σ (ns)
J0437–4715	0.06	50.4	50.4
J1017–7156	4.6	13.7	14.5
J1446–4701	26.0	22.1	34.1
J1545–4550	15.6	36.1	39.3
J1600–3053	2.9	26.6	26.8
J1713+0747	0.8	35.1	35.1
J1744–1134	3.9	41.2	41.4
J1832–0836	3.7	14.2	14.8
J1909–3744	1.2	11.2	11.3
J2241–5236	1.5	15.4	15.5

noise, which is thought to be associated with the intrinsic and stochastic variability in the shape of individual pulses [90]. Such a limitation implies that the timing precision stops improving for the brightest pulsars even when better instruments are used. The level of jitter noise can be approximately estimated with the following relation [91]

$$\sigma_J \approx 0.2W \sqrt{\frac{P}{T_{\text{int}}}}, \quad (30)$$

where T_{int} is the time of integration, W and P are the pulse width and pulse period, respectively. Note that the only way to reduce jitter noise is to increase T_{int} . In comparison, the radiometer noise is given by [89]

$$\sigma_r \approx \frac{W}{S/N} \approx \frac{WS_{\text{sys}}}{S_{\text{mean}} \sqrt{2\Delta f T_{\text{int}}}} \sqrt{\frac{W}{P-W}}, \quad (31)$$

where S/N is the pulse profile signal-to-noise ratio, S_{sys} is the system-equivalent flux density, S_{mean} is the pulsar mean flux density and Δf is the observing bandwidth. We adopt nominal SKA parameters,⁹ $S_{\text{sys}} = 1.8$ Jy, $\Delta f = 770$ MHz and set a fiducial $T_{\text{int}} = 30$ minutes.

Table IV lists white noise budgets (σ_r , σ_J and the total white noise σ) expected in the FAST/SKA era for ten PPTA pulsars that have the lowest value of σ . As one can see, for the SKA, jitter noise will dominate over the radiometer noise for the majority of bright pulsars. In order to realistically estimate the PTA sensitivity in the FAST/SKA era, we use the total white noise given in Table IV plus the intrinsic spin noise (where appropriate) with parameters determined from the Bayesian analysis.

⁹SKA1 system baseline V2 description <https://www.skatelescope.org/>.

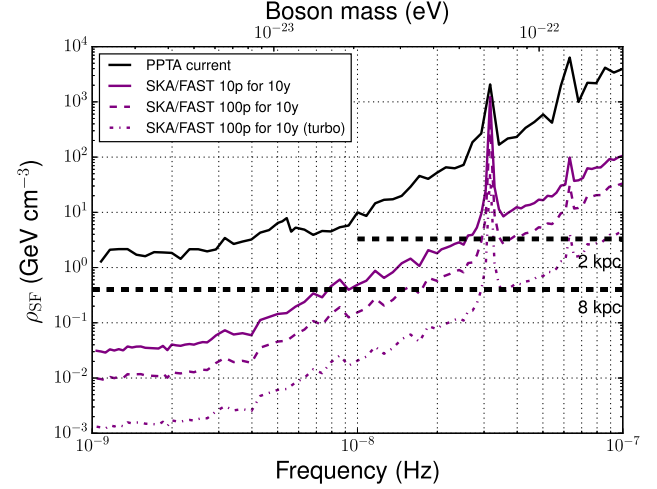


FIG. 4. Upper limits on the dark matter density ρ in the Galaxy. The current PPTA upper limits (black solid line) are shown along with projected limits in the FAST/SKA era (purple lines, all assuming 10-yr data span): (a) 10 pulsars, 14-day cadence, 30-min integration, (b) 100 pulsars, 14-day cadence, 30-min integration, and (c) 100 pulsars, 1-day cadence, 2-hours integration (turbo). The black dashed lines show the dark matter density in the Halo at 8 kpc ($\rho_{\text{SF}} = 0.4 \text{ GeV cm}^{-3}$) and 2 kpc ($\rho_{\text{SF}} = 3.4 \text{ GeV cm}^{-3}$) from the Galactic Center, assuming NFW profile. The 8 kpc line demonstrates the predicted dark matter density, applicable to current PPTA pulsars and the Earth, while the 2 kpc line applies to pulsars located at 2 kpc distance from the Galactic center. For boson masses $m \lesssim 4 \times 10^{-23} \text{ eV}$ the size of the solitonic core becomes larger than 2 kpc [29], and the dark matter density will deviate from the NFW prediction towards higher values (see text for details).

Figure 4 shows forecasted upper limits on the density of FDM in the Galaxy for three cases, all assuming a data span of ten years. Case a) is a conservative PTA that includes only ten pulsars as listed in Table IV and an observing cadence of once every 14 days. Upper limits in this case are obtained by running full Bayesian analysis of simulated data. We analytically scale this limit curve to two more ambitious cases.¹⁰ We increase the number of pulsars to 100 in case (b), leading to a factor of $\sqrt{10}$ improvement. For case (c), we further increase the cadence to once every day and adopt an integration time of two hours, providing another factor of $\sqrt{4} \times 14$ improvement. Case c) might be an interesting option in the SKA era since small radio telescopes (compared to SKA/FAST), such as Parkes, can be dedicated for high-cadence and long integration observations of the brighter pulsars.

As one can see from Fig. 4, we will be able to constrain the contribution of FDM to the local dark matter density below 10% for $m \lesssim 10^{-23} \text{ eV}$ in ten years under the

¹⁰Note that the scaling factor should be a good approximation at high frequencies where red noise plays a less important role.

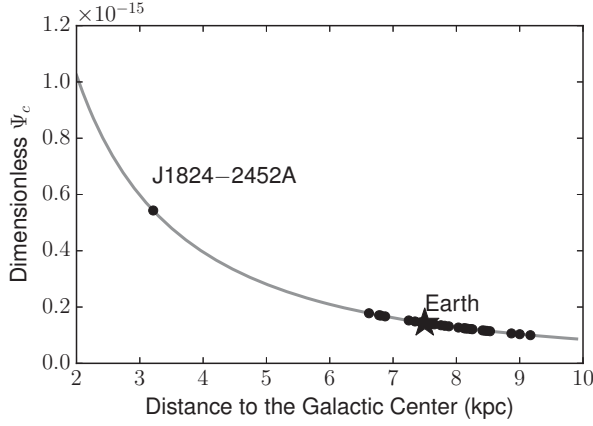


FIG. 5. The amplitude of the expected dark matter signal for different pulsars, assuming NFW dark matter density profile. The mass of the scalar dark matter particles is assumed to be 2×10^{-23} eV.

conservative assumption for SKA sensitivity. However, it is more challenging for boson masses above 10^{-22} eV; we estimate that decade-long observations of hundreds of pulsars timed at nearly daily cadence with precision $\lesssim 20$ ns are necessary to place interesting limits.

There are a couple of ways to improve our analysis. First, the coherence between pulsar terms and Earth terms can be used to enhance the sensitivity. When a pulsar and the Earth are located within a de Broglie wavelength λ_{dB} , the oscillation phases, which have been assumed to be independent in the current analysis, are correlated. However, for $m \gtrsim 10^{-22}$ eV, this effect will have no impact on the current results, since $\lambda_{dB} = 60 \text{ pc}(10^{-22} \text{ eV}/m)$ and no pulsars have been found within 60 pc to the Earth. Another interesting point is that pulsars that are close to each other within λ_{dB} also experience phase-coherent oscillations [36]. We plan to explore these features in a future work.

Second, the oscillation amplitude Ψ_c is proportional to the local dark matter density. Thus, in contrast to the amplitude of the Earth term, the amplitude of the pulsar term varies from pulsar to pulsar; see Eq. (7). In Λ -FDM cosmological simulations [29,36], it was shown that due to wave interference the dark matter forms gritty pattern with typical granule size of around λ_{dB} . When averaged over $\gg \lambda_{dB}$ scales, the periphery (> 1 kpc) density profile is similar to the classical Navarro-Frenk-White (NFW) profile, whereas a distinct density peak is seen in the central regions (usually called solitonic core, see [29] for details).

Figure 5 shows the expected signal amplitude for PPTA pulsars assuming the NFW dark matter density profile [92] with parameters from [93]. As one can see, pulsars closer to the Galactic center provide better sensitivity to the dark matter signal. The amplitude of the dark matter signal becomes even larger than NFW prediction within the

central solitonic core ($\lesssim 1$ kpc) [36]. For the current PPTA sample, PSR J1824–2452A is expected to have the largest signal amplitude, a factor of ~ 5 larger than other pulsars.¹¹ However, this pulsar is nearly the worst timer in PPTA (see Table I and Fig. 1). Existing and future pulsar surveys might help find high quality millisecond pulsars close to the Galactic Center and thus provide better sensitivity to the dark matter searches [94].

VI. CONCLUSIONS

Pulsar timing is a powerful tool to study a wide variety of astrophysical phenomena. By exploiting precision timing observations from an array of the most stable millisecond pulsars, PTAs allow us to measure minute correlations in the ToAs of different pulsars. Like continuous GWs from individual supermassive binary black holes, FDM in the Galaxy produces periodic variations in pulsar ToAs. We perform a search for evidence of ultralight dark matter in the latest PPTA data set. Finding no statistically significant signals, we place upper limits on the dark matter density: for boson mass $m \lesssim 10^{-23}$ eV, our analysis constrains the density below 6 GeV cm^{-3} with 95% confidence; at $m \approx 10^{-22}$ eV, our upper limits remain 3 orders of magnitude above the local dark matter density 0.4 GeV cm^{-3} inferred from kinematics measurements of stars in the Galaxy [58].

We derived the noise properties of PPTA data and obtain dark matter constraints using both Bayesian and Frequentist methods. Our upper limits from the two methods are broadly consistent. We reanalyzed the NANOGrav 5-yr data set and found that the PPTA data result in a factor of 2 to 5 improvement in dark matter constraints. We studied potential systematics due to SSE errors in our analysis and found that the search for ultralight dark matter is insensitive to such errors. We have ignored effects from instabilities in terrestrial time standards; such clock errors produce a monopolar broad-band noise [95]. Whereas this effect should be distinguishable from the sinusoidal ToA variations due to ultralight dark matter, one needs to include it in a future study to quantitatively assess the impact.

We forecasted the PTA sensitivity in the FAST/SKA era while accounting for realistic noise levels. We found that observing the ten best PPTA pulsars for ten years would constrain the density of FDM below 0.05 GeV cm^{-3} for $m \lesssim 10^{-23}$ eV, about 10% of measured total dark matter density. At $m \approx 2 \times 10^{-23}$ eV, our projected limit is around

¹¹The density of the scalar field dark matter in globular clusters is not expected to deviate significantly from the general trend as λ_{dB} is larger than typical sizes of globular clusters. Thus, the amplitude of the oscillation at J1824–2452A, located in a globular cluster, is expected to follow the NFW prediction.

0.4 GeV cm^{-3} ; for higher boson masses, the upper limits increase as $\sim m^3$. Above $m \approx 10^{-22} \text{ eV}$, the projected limits are more than 1 order of magnitude above the local dark matter density. To place interesting limits in this mass range, an ambitious timing program in which hundreds of pulsars timed with daily cadence and high precision ($\lesssim 20 \text{ ns}$) for more than a decade is required. Finally, we point out that high-quality pulsars in the vicinity of the Galactic Center will be ideal tools to test the fuzzy dark matter hypothesis.

ACKNOWLEDGMENTS

The Parkes radio telescope is part of the Australia Telescope National Facility which is funded by the Commonwealth of Australia for operation as a National Facility managed by CSIRO. N. K. P. acknowledges the support from IMPRS Bonn/Cologne and the Bonn-Cologne Graduate School (BCGS). X. Z., M. B., D. J. R., R. M. S. and L. W. are supported by ARC CE170100004. X. Z. and L. W. are additionally supported by ARC DP150102988. L. H. is supported in part by NASA NXX16AB27G and DOE DE-SC0011941. Work at N. R. L. is supported by NASA. P. D. L. is supported through ARC FT160100112 and ARC DP180103155. M. B., S. O. and R. S. acknowledge support through the ARC Laureate Fellowship Grant No. FL150100148. J. W. is supported by Qing Cu Hui of Chinese Academy of Sciences (CAS). We acknowledge the Institute for Theoretical and Experimental Physics and, in

particular, Prof. Sergey Blinnikov for providing computing facilities. The authors would like to thank Dr. Maxim Pshirkov, Dr. Mikhail Ivanov, Dr. Nicolas Caballero and Dr. David Champion for fruitful discussions. We would like to thank the anonymous referees for useful comments.

APPENDIX A: EARTH-TERM LIMITS AND EFFECTS OF SSE

When searching for continuous GWs in PTA data, it is common to use only the Earth terms. Similarly, for the case of scalar field dark matter, we can include in the analysis only Earth terms in Eq. (6). Although pulsar and Earth terms lie in the same frequency bin, we expect that for a sufficiently large set of pulsars, pulsar terms will be averaged out, as they all have different phases. In the left panel of Fig. 6, we compare the Frequentist upper limits on the density of scalar field dark matter ρ_{SF} when only Earth terms are considered (black dashed) and when the full signal is used (purple solid). We find that both limits are comparable to each other. The noisy features in the (purple) solid curve are due to the amplitude modulation of pulsar terms; see Eq. (9).

We also demonstrate the effects of SSE errors. In the right panel of Fig. 6, we show the upper limits obtained when DE418 and DE435 planetary ephemeris are used. The results with fixed ephemeris are overplotted with upper limits obtained with `BayesEphem` model, which accounts for uncertainties in the SSE. We see that the results are comparable, indicating the search for FDM signal, or continuous waves in general, is insensitive to SSE errors.

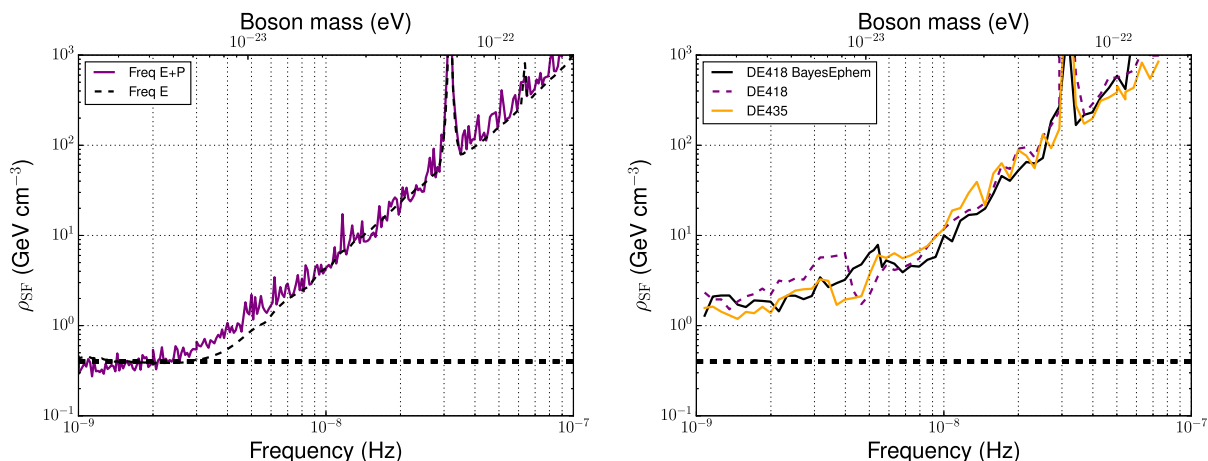


FIG. 6. Upper limits on the density of fuzzy dark matter ρ_{SF} in the Galaxy, as a function of frequency (boson mass). *Left*: results from Frequentist analysis when only the Earth term is included (Freq E) or both terms are used (Freq E + P). *Right*: Bayesian upper limits when SSE parameters are included in the search (BayesEphem), or using fixed DE418 and DE435 planet ephemerids. The horizontal black dashed line marks the measured local dark matter density 0.4 GeV cm^{-3} [58].

APPENDIX B: NOISE PROPERTIES FOR SIX PPTA PULSARS

Figure 7 shows results of the Bayesian noise parameter estimation, described in Sec. III C 1, for the six most sensitive pulsars in the current PPTA data set.

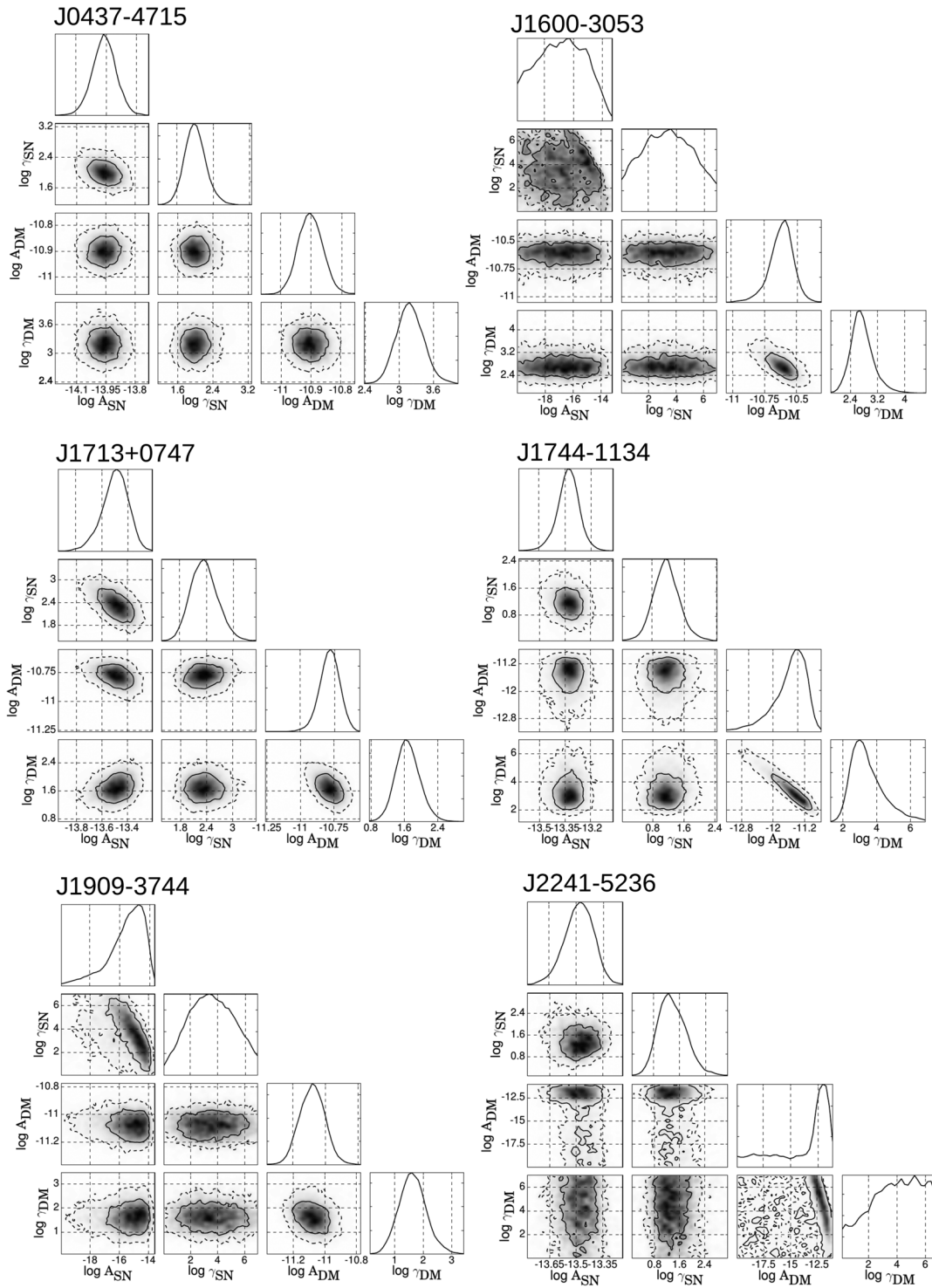


FIG. 7. The one- and two-dimensional marginalized posterior distributions for the log-amplitude and slope of the DM and spin noises for the six best pulsars in the current PPTA data set.

- [1] F. Zwicky, *Helv. Phys. Acta* **6**, 110 (1933).
- [2] F. Zwicky, *Astrophys. J.* **86**, 217 (1937).
- [3] S. Smith, *Astrophys. J.* **83**, 23 (1936).
- [4] L. V. E. Koopmans and T. Treu, *Astrophys. J.* **583**, 606 (2003).
- [5] D. Clowe, A. Gonzalez, and M. Markevitch, *Astrophys. J.* **604**, 596 (2004).
- [6] M. Tegmark *et al.*, *Astrophys. J.* **606**, 702 (2004).
- [7] P. A. R. Ade *et al.* (Planck Collaboration), *Astron. Astrophys.* **594**, A13 (2016).
- [8] G. Bertone, D. Hooper, and J. Silk, *Phys. Rep.* **405**, 279 (2005).
- [9] J. R. Primack, *Ann. Phys. (Berlin)* **524**, 535 (2012).
- [10] M. Battaglieri *et al.*, arXiv:1707.04591.
- [11] A. Arvanitaki, S. Dimopoulos, S. Dubovsky, N. Kaloper, and J. March-Russell, *Phys. Rev. D* **81**, 123530 (2010).
- [12] L. Hui, J. P. Ostriker, S. Tremaine, and E. Witten, *Phys. Rev. D* **95**, 043541 (2017).
- [13] J. Preskill, M. B. Wise, and F. Wilczek, *Phys. Lett.* **120B**, 127 (1983).
- [14] L. F. Abbott and P. Sikivie, *Phys. Lett.* **120B**, 133 (1983).
- [15] M. Dine and W. Fischler, *Phys. Lett.* **120B**, 137 (1983).
- [16] P. Srceek and E. Witten, *J. High Energy Phys.* **06** (2006) 051.
- [17] W. Hu, R. Barkana, and A. Gruzinov, *Phys. Rev. Lett.* **85**, 1158 (2000).
- [18] J. S. Bullock and M. Boylan-Kolchin, *Annu. Rev. Astron. Astrophys.* **55**, 343 (2017).
- [19] R. Hložek, D. J. E. Marsh, and D. Grin, *Mon. Not. R. Astron. Soc.* **476**, 3063 (2018).
- [20] V. Iršič, M. Viel, M. G. Haehnelt, J. S. Bolton, and G. D. Becker, *Phys. Rev. Lett.* **119**, 031302 (2017).
- [21] T. Kobayashi, R. Murgia, A. De Simone, V. Iršič, and M. Viel, *Phys. Rev. D* **96**, 123514 (2017).
- [22] J. D. Bowman, A. E. E. Rogers, R. A. Monsalve, T. J. Mozdzen, and N. Mahesh, *Nature* **555**, 67 (2018).
- [23] A. Schneider, *Phys. Rev. D* **98**, 063021 (2018).
- [24] A. Lidz and L. Hui, *Phys. Rev. D* **98**, 023011 (2018).
- [25] J. M. Sullivan, S. Hirano, and V. Bromm, *Mon. Not. R. Astron. Soc.* **481**, L69 (2018).
- [26] E. Calabrese and D. N. Spergel, *Mon. Not. R. Astron. Soc.* **460**, 4397 (2016).
- [27] H. Deng, M. P. Hertzberg, M. H. Namjoo, and A. Masoumi, *Phys. Rev. D* **98**, 023513 (2018).
- [28] N. Bar, D. Blas, K. Blum, and S. Sibiryakov, arXiv:1805.00122.
- [29] H.-Y. Schive, T. Chiueh, and T. Broadhurst, *Nat. Phys.* **10**, 496 (2014).
- [30] P. Mocz and S. Succi, *Phys. Rev. E* **91**, 053304 (2015).
- [31] J. Veltmaat and J. C. Niemeyer, *Phys. Rev. D* **94**, 123523 (2016).
- [32] M. Nori and M. Baldi, *Mon. Not. R. Astron. Soc.* **478**, 3935 (2018).
- [33] J. Veltmaat, J. C. Niemeyer, and B. Schwabe, *Phys. Rev. D* **98**, 043509 (2018).
- [34] A. Khmelnitsky and V. Rubakov, *J. Cosmol. Astropart. Phys.* **02** (2014) 019.
- [35] N. K. Porayko and K. A. Postnov, *Phys. Rev. D* **90**, 062008 (2014).
- [36] I. De Martino, T. Broadhurst, S.-H. H. Tye, T. Chiueh, H.-Y. Schive, and R. Lazkoz, *Phys. Rev. Lett.* **119**, 221103 (2017).
- [37] D. Blas, D. L. Nacir, and S. Sibiryakov, *Phys. Rev. Lett.* **118**, 261102 (2017).
- [38] M. V. Sazhin, *Sov. Astron.* **22**, 36 (1978).
- [39] S. Detweiler, *Astrophys. J.* **234**, 1100 (1979).
- [40] R. W. Hellings and G. S. Downs, *Astrophys. J.* **265**, L39 (1983).
- [41] R. S. Foster and D. C. Backer, *Astrophys. J.* **361**, 300 (1990).
- [42] R. N. Manchester *et al.*, *Pub. Astron. Soc. Aust.* **30**, e017 (2013).
- [43] M. A. McLaughlin, *Classical Quantum Gravity* **30**, 224008 (2013).
- [44] M. Kramer and D. J. Champion, *Classical Quantum Gravity* **30**, 224009 (2013).
- [45] G. Hobbs *et al.*, *Classical Quantum Gravity* **27**, 084013 (2010).
- [46] J. P. W. Verbiest *et al.*, *Mon. Not. R. Astron. Soc.* **458**, 1267 (2016).
- [47] R. M. Shannon *et al.*, *Science* **342**, 334 (2013).
- [48] X.-J. Zhu *et al.*, *Mon. Not. R. Astron. Soc.* **444**, 3709 (2014).
- [49] J. B. Wang *et al.*, *Mon. Not. R. Astron. Soc.* **446**, 1657 (2015).
- [50] R. M. Shannon *et al.*, *Science* **349**, 1522 (2015).
- [51] P. B. Demorest *et al.*, *Astrophys. J.* **762**, 94 (2013).
- [52] J. Ellis and R. van Haasteren, jellis18/pal2: Pal2 (2017).
- [53] S. Taylor and P. T. Baker, stevertaylor/nx01 1.2 (2017).
- [54] V. Brdar, J. Kopp, J. Liu, P. Prass, and X.-P. Wang, *Phys. Rev. D* **97**, 043001 (2018).
- [55] X.-J. Zhu, L. Wen, J. Xiong, Y. Xu, Y. Wang, S. D. Mohanty, G. Hobbs, and R. N. Manchester, *Mon. Not. R. Astron. Soc.* **461**, 1317 (2016).
- [56] J. Bovy and S. Tremaine, *Astrophys. J.* **756**, 89 (2012).
- [57] J. I. Read, *J. Phys. G* **41**, 063101 (2014).
- [58] S. Sivertsson, H. Silverwood, J. I. Read, G. Bertone, and P. Steger, *Mon. Not. R. Astron. Soc.* **478**, 1677 (2018).
- [59] R. N. Manchester, G. B. Hobbs, A. Teoh, and M. Hobbs, *Astron. J.* **129**, 1993 (2005).
- [60] L. Lentati *et al.*, *Mon. Not. R. Astron. Soc.* **458**, 2161 (2016).
- [61] W. Folkner, E. Standish, J. Williams, and D. Boggs, Jet Propulsion Laboratory, Memorandum IOM Report No. 343R-08-003, 2007.
- [62] G. B. Hobbs, R. T. Edwards, and R. N. Manchester, *Mon. Not. R. Astron. Soc.* **369**, 655 (2006).
- [63] R. T. Edwards, G. B. Hobbs, and R. N. Manchester, *Mon. Not. R. Astron. Soc.* **372**, 1549 (2006).
- [64] R. van Haasteren, Y. Levin, P. McDonald, and T. Lu, *Mon. Not. R. Astron. Soc.* **395**, 1005 (2009).
- [65] R. van Haasteren and Y. Levin, *Mon. Not. R. Astron. Soc.* **428**, 1147 (2013).
- [66] W. H. Press, S. A. Teukolsky, W. T. Vetterling, and B. P. Flannery, *Numerical Recipes in C*, Vol. 2 (Cambridge University Press, Cambridge, England, 1996).
- [67] P. E. Boynton, E. J. Groth, D. P. Hutchinson, G. P. Nanos, Jr., R. B. Partridge, and D. T. Wilkinson, *Astrophys. J.* **175**, 217 (1972).

- [68] R. Blandford, R. Narayan, and R. W. Romani, *J. Astrophys. Astron.* **5**, 369 (1984).
- [69] G. Hobbs, A. G. Lyne, and M. Kramer, *Mon. Not. R. Astron. Soc.* **402**, 1027 (2010).
- [70] W. W. Hager, *SIAM Rev.* **31**, 221 (1989).
- [71] R. van Haasteren and M. Vallisneri, *Mon. Not. R. Astron. Soc.* **446**, 1170 (2015).
- [72] Z. Arzoumanian *et al.*, *Astrophys. J.* **794**, 141 (2014).
- [73] L. Lentati, P. Alexander, M. P. Hobson, S. Taylor, J. Gair, S. T. Balan, and R. van Haasteren, *Phys. Rev. D* **87**, 104021 (2013).
- [74] L. Lentati, P. Alexander, M. P. Hobson, F. Feroz, R. van Haasteren, K. J. Lee, and R. M. Shannon, *Mon. Not. R. Astron. Soc.* **437**, 3004 (2014).
- [75] F. Feroz, M. P. Hobson, and M. Bridges, *Mon. Not. R. Astron. Soc.* **398**, 1601 (2009).
- [76] F. Feroz, M. P. Hobson, E. Cameron, and A. N. Pettitt, [arXiv:1306.2144](https://arxiv.org/abs/1306.2144).
- [77] M. J. Keith *et al.*, *Mon. Not. R. Astron. Soc.* **429**, 2161 (2013).
- [78] W. A. Coles *et al.*, *Astrophys. J.* **808**, 113 (2015).
- [79] X. P. You *et al.*, *Mon. Not. R. Astron. Soc.* **378**, 493 (2007).
- [80] W. Coles, G. Hobbs, D. J. Champion, R. N. Manchester, and J. P. W. Verbiest, *Mon. Not. R. Astron. Soc.* **418**, 561 (2011).
- [81] S. Babak *et al.*, *Mon. Not. R. Astron. Soc.* **455**, 1665 (2016).
- [82] Z. Arzoumanian *et al.*, *The Astrophysical Journal* **859**, 47 (2018).
- [83] C. Tiburzi, G. Hobbs, M. Kerr, W. A. Coles, S. Dai, R. N. Manchester, A. Possenti, R. M. Shannon, and X. P. You, *Mon. Not. R. Astron. Soc.* **455**, 4339 (2016).
- [84] R. C. Eberhart and J. Kennedy, in *Proceedings of the Sixth International Symposium on Micro Machine and Human Science*, Vol. 1, New York, NY (IEEE, Piscataway, NJ, 1995), pp. 39–43.
- [85] Y. Wang, S. D. Mohanty, and F. A. Jenet, *Astrophys. J.* **815**, 125 (2015).
- [86] R. Nan, D. Li, C. Jin, Q. Wang, L. Zhu, W. Zhu, H. Zhang, Y. Yue, and L. Qian, *Int. J. Mod. Phys. D* **20**, 989 (2011).
- [87] M. Bailes *et al.*, *Proc. Sci. MeerKAT2016* (**2018**) 011.
- [88] T. J. W. Lazio, *Classical Quantum Gravity* **30**, 224011 (2013).
- [89] G. Hobbs, S. Dai, R. N. Manchester, R. M. Shannon, M. Kerr, K. J. Lee, and R. Xu, [arXiv:1407.0435](https://arxiv.org/abs/1407.0435).
- [90] S. Osłowski, W. van Straten, G. B. Hobbs, M. Bailes, and P. Demorest, *Mon. Not. R. Astron. Soc.* **418**, 1258 (2011).
- [91] R. M. Shannon and J. M. Cordes, *Astrophys. J.* **761**, 64 (2012).
- [92] J. F. Navarro, C. S. Frenk, and S. D. M. White, *Astrophys. J.* **462**, 563 (1996).
- [93] Y. Sofue, *Publ. Astron. Soc. Jpn.* **64**, 75 (2012).
- [94] M. Kramer, D. C. Backer, J. M. Cordes, T. J. W. Lazio, B. W. Stappers, and S. Johnston, *New Astron. Rev.* **48**, 993 (2004).
- [95] G. Hobbs *et al.*, *Mon. Not. R. Astron. Soc.* **427**, 2780 (2012).